PROGRESS TOWARD MINIATURE SPACE WEATHER STATIONS

Dr. Linda Habash Krause
United States Air Force Academy, Department of Physics

Dr. Federico A. Herrero
NASA Goddard Space Flight Center, Detector Systems Branch

Dr. John Champion
Johns Hopkins University, Applied Physics Laboratory

LtCol Francis K. Chun
United States Air Force Academy, Department of Physics

Mr. Dean D. Aalami
Space Instruments, Inc.

Abstract – Responding to a growing need to specify (nowcast) and predict (forecast) hazardous space weather events and their deleterious effects on space systems, the authors have developed a prototype suite of instruments that would serve as a key component of a miniature space weather station. Space environment data have been gathered over several solar cycles, and though these data assist space operators in "predicting" hazards to space systems based upon derived climatology, no true forecasting ability yet exists. (As an analogy, consider for example the difference between tropospheric weather reports based on data-driven forecast models versus a "prediction" based upon the average temperature for a given city on a given date over the last hundred years.) True space weather forecasting models require assimilation of space-based *in situ* data into physics-based models. Data collection of fundamental characteristics, such as plasma density and temperature, neutral wind and bulk ion velocity, and electric and magnetic field strengths is required at multiple grid points, similar to tropospheric weather stations that measure temperature, wind speed, humidity, *etc*. Recent breakthroughs in fabrication techniques have enabled the development of a suite of instruments that is comprised of 16 individual analyzers, each of which is capable of providing a unique measurement of a partially ionized space environment. The suite is designed to measure ion spectra differential in energy and angle, bulk ion velocities, bulk neutral velocities, and ion and neutral mass spectra. Preliminary functional testing has indicated the ability to resolve He, O, O_2, and Ar; separation of O_2 and N_2 has proved elusive to date. In the prototype suite, the instrument assembly that houses the 16 analyzers is stacked to a conventional Printed Circuit Board (PCB) with anodes and circuit components and an electronics enclosure containing a high voltage power supply, amplifier Application Specific Integrated Circuits (ASICs), and a Rad Hard microcontroller. The suite configuration, including all aforementioned components, has a total volume of 7 cm × 7 cm × 4 cm = 196 cm^3, a mass of 400 g, and a peak power requirement of 1.5 W (for neutral measurements). Challenges inherent to miniaturization of spacecraft capable of providing real utility are identified and addressed.

1. Introduction and Background

As agencies within the military, civilian, and private sectors increasingly rely on space-based systems as core components of their operational infrastructure, the need for a space weather effects warning system is growing in both importance and urgency. A variety of space environmental conditions have the potential to contribute to isolated systems anomalies as well as long term degradation. Effects and consequences range in severity; for example, a mild surface charging event of a geosynchronous satellite may be nothing more than a nuisance in the form of a plasma measurement offset, whereas a time-critical communications outage could lead to disaster for operational field personnel

Recognizing the need for development of a strategic plan to address this issue, several top level government studies have produced key documents containing guidelines to lead a coherent effort. The National Space Weather Program (NSWP), consisting of several government organizations such as the Departments of Defense (DoD), Commerce (DoC), Interior (DoI), and Energy (DoE), the National Aeronautics and Space Administration (NASA), and the National Science Foundation (NSF), drafted an implementation plan [*NSWP, 2000*] in the late 1990s to address the vulnerability of space assets, to centralize the scientific and technological objectives necessary for reduction or elimination of those vulnerabilities, and to develop a coherent space weather research and development program to attain those objectives. Key elements identified in the NSWP implementation plan (NSWPIP) include:

1. *Forecast and Specification Services*. The goal is to design and implement an operational system that is comparable in precision and accuracy to those services associated with terrestrial weather.
2. *Basic Research*. Here, investigators focus on the physics and chemistry of the upper atmosphere, thermosphere, ionosphere, magnetosphere, solar wind, the sun, and all coupling processes necessary for description of a seamless environment.
3. *Observations*. Measurement objectives drive instrumentation and operational requirements necessary to improve coverage of data-sparse regions of space.
4. *Modeling*. Physics-based models are increasing in sophistication through the implementation of advanced techniques in data assimilation, adaptive grids, *etc*.
5. *Technology Transition and Integration*. Validated systems are transitioned into the operations centers for rapid and effective dissemination amongst primary users.

With this paper the authors present recent progresses in technology research and development that support the NSWPIP *Observations* element. A brief review of space weather processes and associated effects is presented in Section 2. As an example of break-through technology, the Flat Plasma Spectrometer (FLAPS), a suite of miniaturized space plasma sensors and control electronics, is discussed in Section 3. Issues associated with miniaturization are presented in Section 4. Section 5 contains concluding remarks and recommendations for future work.

2. Space Weather and Associated Effects on Technology Infrastructure

It is well known that the space environment in which our satellites operate is permeated with particles and radiation subject to complex processes that complicates forecasting of space environment interactions. Figure 1 shows an overview of the near-Earth space environment with three common spacecraft orbits: Geosynchronous Earth Orbit (GEO), Medium Earth Orbit (MEO), and Polar Earth Orbit (PEO). These orbits and their unique environments are described in detail in the following sections. A brief summary of common space weather effects is also described.

Space Environments

Communication satellites are often located at an altitude such that their period of revolution matches that of the Earth's rotation. This so-called Geosynchronous Earth Orbit (GEO) has an orbital radius of 6.6 earth radii, corresponding to an altitude of ~36,000 km. The quiescent GEO environment is typically characterized as a Maxwellian plasma with plasma density and temperature on the order of 10^8 m^{-3} and 0.1 eV, respectively. During periods of significant geomagnetic activity, the environment is more appropriately represented as a two-temperature Maxwellian, shown graphically in Figure 2 and given quantitatively as:

$$f(v) = \left(\frac{m}{2p}\right)^{3/2}\left[\frac{n_1}{(kT_1)^{3/2}}\exp\left(\frac{-mv^2}{2kT_1}\right) + \frac{n_2}{(kT_2)^{3/2}}\exp\left(\frac{-mv^2}{2kT_2}\right)\right]$$

Here, $f(v)$ represents the speed (v) probability distribution, m is the electron mass, and (n_1, kT_1) and (n_2, kT_2) are the density/temperature pairs of the superimposed particle populations.

Though a spacecraft located at GEO is almost always exposed to sunlight (eclipse periods

account for less than 1% of a satellite's operational time on orbit), the particle environment varies significantly with respect to phase, especially during magnetospheric activity. For example, during a geomagnetic storm, solar wind compression of the Earth's magnetosphere occasionally results in a magnetopause that is compressed Earthward of a GEO orbit; spacecraft near the noon meridian may experience direct exposure to the solar wind (see Figure 3). Alternatively, magnetospheric substorms are often accompanied by injection of an energetic (E ~ 10 keV) ion and electron population in the pre- and post-midnight sectors of the GEO environment, respectively (see Figure 4). Defense Satellite Communication System (DSCS III) observations of such electron injection are shown with the black trace in the bottom panel of Figure 3. The electron injection in the post-midnight sector is known to be particularly problematic, as will be shown in the section covering space weather effects.

Medium Earth Orbit (MEO) is a term that loosely refers to that region of space near 20,000 km in altitude occupied by the ubiquitous Global Positioning System (GPS) spacecraft. Arguably the harshest region within the near-Earth space environment in terms of spacecraft penetrating radiation, the MEO regularly transits the outer Van Allen radiation belt, which tends to be dominated by high energy (E ~ 1 MeV) electrons (see Figure 5). The energetic charged particles originate from a variety of sources, including direct entry from the solar wind, polar ionospheric outflow, and cosmic ray particle albedo. Their trajectories are dominated by single particle motion, including gyrorotation about the terrestrial magnetic field, bounce motion longitudinally along the magnetic field with reflections at hemispherically conjugate mirror points, and cross-field drift azimuthally about the Earth due to the curvature of the magnetic field. These motions are illustrated in Figure 6. The nominally trapped population of charged particles is subject to loss processes as well, such as pitch angle scattering into the magnetospheric loss cone and subsequent precipitation at auroral latitudes.

The Low Earth Orbit (LEO) is used to describe a low altitude ($z < 1000$ km) and low latitude ($\phi < 30°$) space environment. The ionosphere in this region can be specified nominally as a one temperature Maxwellian plasma with a temperature and density on the order of 0.1 eV and $10^{10} - 10^{12}$ m^{-3}, respectively. Generally, the region is well-protected from high energy charged particles (E > 100 keV) with one prominent exception: the South Atlantic Anomaly (SAA). The SAA is a "weakness" in the Earth's internal magnetic field which allows particle entry to lower altitudes (see Figure 7). It is a manifestation of higher order moments of the Earth's magnetic field, and particles which would normally reflect off their mirror point in this region would penetrate to lower altitudes along lines of constant magnetic field strength.

Localized enhancements and depletions in the ambient thermal plasma population occur as a result of certain physical processes particular to the equatorial region. For example, the Equatorial Appleton Anomaly (EAA) is driven in the dayside by plasma subject to a strong upward E (Eastward) cross B (northward) drift. The upward drifting plasma reaches a peak altitude and diffuses downward toward higher latitudes, resulting in peak plasma densities localized in bands near 15°-20° in magnetic latitude (see Figure 8). As another example, there is significant plasma turbulence caused by the Generalized Rayleigh Taylor (GRT) instability, a plasma instability resulting from a heavy plasma residing on top of a light plasma in a gravitational field. Near the equator, and in the post sunset F region ionosphere, the orientation of the electric and magnetic fields favor GRT onset and growth. Localized depletions in plasma density result, varying in depth up to three orders of magnitude (*i.e.*, reduced to 0.1% of the ambient plasma density) and in spatial scale size from cm up to 100s of km.

The Polar Earth Orbit (PEO) is a low altitude ($z <$ 1000 km), high latitude ($f > 60°$) orbit often used for weather satellites, such as the Defense Meteorological Satellite Program (DMSP). In addition to the processes associated with transit of the low latitude ionosphere described in the previous section, a PEO satellite is subject to additional complexity in its traversal through a variable and intricate polar and auroral ionospheric environment. *Fontheim et al.* [1982] characterizes the plasma electron distribution

during auroral activity as a superposition of three fundamental distributions: a Gaussian to represent the magnetic field aligned auroral electron beams, a Maxwellian to designate thermal background plasma, and a power law spectrum to specify the secondary and backscattered electrons resulting from interaction between the auroral electron beam and the background neutral atmosphere. The resulting spectrum takes the form:

$$f(E) = f_G + f_M + f_P$$

$$= A_G E \exp\left[-\left(\frac{E - E_o}{\Delta}\right)^2\right]$$

$$+ \frac{n_e}{\sqrt{2p^3 m_e}} \frac{E}{q^{3/2}} e^{-E/q}$$

$$+ A_P E^{-a} \quad \text{for } (E_{PL} \le E \le E_{PH})$$

where:

- f = electron flux
- E = particle energy
- E_o = beam central energy
- Δ = beam energy distribution width
- n_e = ambient plasma density
- m_e = electron mass
- q = plasma temperature
- a = power law factor
- A_G and A_P = relative fraction of plasma population of Gaussian and power law forms, respectively
- E_{PL} and E_{PH} = lower and upper bounds of the energy range at which it is appropriate to specify the electron distribution as a power law.

Barker [1986] derived the following distribution parameters for the Fontheim form:

E_{PL} = 10-20 eV
E_{PH} ~ 1 keV
a = 2.5-4.5
Δ = 1-10 keV
E_o = 5-15 keV
$n_e = 10^5$-10^7 m^{-3}
q = 1-20 keV

A sample Fontheim spectrum appears in Figure 9.

Space Weather Effects on Satellite Systems

Spacecraft surfaces exposed to a charged particle or ultraviolet radiation environment are prone to accumulation of static charge buildup. This set of spacecraft environment interactions is collectively known as spacecraft charging. Satellite frame charging results when the excess charge resides within the spacecraft frame structure, resulting in a potential that floats with respect to the background plasma potential [*DeForest*, 1972]. Differential surface charging results when charge builds up on a surface dielectric, resulting in a potential that is significantly different from the spacecraft's frame or other components on the spacecraft's surface [*Mizera*, 1980]. Electrons with energies of 10s of keV are known to contribute to frame and differential surface charging [*Mullen et al.*, 1986]. Deep dielectric charging occurs when energetic electrons (E > 100 keV) are deposited the volume of an internal dielectric satellite component [*Fredrickson et al.*, 1993]. GEO and PEO spacecraft are often subject to surface charging due to the significant presence of electrons with energies ~ 10 keV. For example, as illustrated in Figure 10, GEO satellite operational anomalies have been statistically correlated with frame charging probability in the post-midnight sector, where energetic electron injection is commonly associated with geomagnetic activity [*Habash Krause et al.*, 2000]. MEO and LEO spacecraft are more prone to deep dielectric charging due to the regular exposure to energetic (E > 100 keV) electrons. (Though PEO spacecraft are exposed to the SAA, their frequency of traversal is not as high as a LEO spacecraft.)

The term Single Event Effects (SEE) is given to a set of processes associated with state changes within an electronics device due to energetic particle-induced ionization within the device. For example, creation of electron-hole pairs within a depletion region of a semiconductor device may lead to a transient pulse that propagates through the circuitry, state changes in memory cells or registers, or other uncontrolled processes. A Single Event Upset (SEU) is the least damaging of these effects. An SEU is a temporary state change

in which device logic experiences a "bit flip" or logic negation that is short lived and usually self-correcting [*Binder et al.*, 1975]. A Single Event Latchup (SEL) is more serious and potentially more damaging in that, whereas it is similar to an SEU in term of the negation process, the state change is latched, maintaining the new state until the device receives a command to restore the bit to its nominal state [*Kolasinski et al.*, 1979]. A Single Event Burnout (SEB) is the most deleterious of the SEE processes. An SEB may occur if the amount of charge induced in the device results in a current that exceeds the limitations of the device, causing permanent destruction of the junction [*Waskiewicz et al.*, 1986]. Spacecraft in all regions of space are susceptible to SEE processes, though satellites in MEO are particularly at risk due to long-term exposure to energetic charged particles ($E \sim 1$ MeV).

The predominant effect of the neutral atmosphere on PEO and LEO spacecraft is the reduction of orbital energy due to atmospheric drag. Quantitatively, the magnitude of the drag acceleration varies linearly with atmospheric density; because the density increases exponentially with decreasing altitude, a spacecraft can rapidly deorbit if it is without sufficient propulsion for orbital boosting. Any space weather process that significantly affects the neutral density of the atmosphere has the potential to affect satellite drag. In particular, fluctuations in solar radiation absorbed by the Earth's atmosphere induce variability in the heating and expansion of the upper atmosphere at PEO and LEO satellite altitudes. PEO spacecraft are subject to additional variability due to high latitude ionospheric heating caused by strong electric currents in the resistive plasma (the so called Joule heating effect). Increases in solar radiation and Joule heating are associated with high levels of solar and geomagnetic activity, respectively. Typically, solar radiation dominates upper atmospheric heating even during significant geomagnetic storms. However, *Knipp et al.* [2002], demonstrated that the variability in upper atmospheric heating was dominated by geomagnetic heating (joule heating and energetic particle deposition) during the strongest 15 geomagnetic storms of the last 2.3 solar cycles (26 years).

Space Weather Effects on Communication/Navigation Systems

Unmagnetized plasma, a frequency-dispersive medium, has an index of refraction which varies monotonically with the plasma density N_e according to the following equation:

$$m(w) = \sqrt{1 - \frac{N_e e^2}{e_o m_e w^2}}$$

where e is the electronic charge, m_e is the electron mass, and e_o is the permittivity of free space. The expression $N_e e^2 / e_o m_e \equiv w_p$ quantifies a unique property of the plasma and is defined as the characteristic plasma frequency of the medium. Generally, a radio wave with frequency greater than the plasma frequency will propagate through the plasma medium, whereas a wave with frequency less than the plasma frequency will be reflected by the medium. Thus, ground to satellite communication systems rely on signals with frequencies in the former category, whereas ground to ground links relying on so-called "sky wave" propagation chose signals in the latter category[1]. It would seem that designing systems for effective propagation of radio waves would be a straightforward process of frequency selection. However, even with proper selection of frequencies necessary for transionospheric propagation, signals nonetheless may be distorted due to irregularities within the ionosphere. With this section, we focus on space weather effects on ionospheric radiowave propagation.

Anomalous absorption of radio waves occurs in regions where the product of electron density and the electron-neutral collision frequency is maximized. In particular, increases in solar radiation may enhance ionization in the low latitude D region ionosphere, whereas increases in energetic particle deposition through magnetic field aligned auroral beams may enhance ionization in the high latitude D region ionosphere. In both cases, ionospheric radio waves are subject to increased absorption: the D

[1] Amateur radio operators often refer to the plasma frequency as the "Maximum Useable Frequency", or MUF, for sky wave propagation. Signals above this frequency propagate beyond the ionosphere and are thus not received by long distance stations.

region plasma responds to electromagnetic waves in the form of oscillatory motion, but due to the frequent collisions with the background neutrals, much of the energy is lost due to heating and momentum exchange. High latitude absorption is commonly known as Polar Cap Absorption (PCA); PCA events are a subset of what are collectively known as D region absorption events.

Scintillations may result from radio waves propagating through a plasma that is permeated with sharp, localized depletions or enhancements in plasma density. Consider the following optical analogy. Though an object may be clearly visible when looking at it in air, and the same object may be visible when viewed underwater (with a good pair of goggles), the object may not be seen clearly when viewed underwater within a Jacuzzi filled with air bubbles. The differential refraction of light waves scattered by sharp anisotropies in the refractive index precludes clear visibility of the object. Extending this concept, the differentially scattered radio waves experience irregular diffraction that ultimately distorts the signal in both phase and amplitude.

The phase screen approximation is used to illustrate scintillation in its simplest form. Figure 11 illustrates this process. A plane wave is incident onto a thin, irregularly shaped layer of a uniform index of refraction. The red arrows represent the wave vector of the incident and transmitted wave. We consider that the plane and transmitted waves are composed of an infinite series of wavelets and apply Huygen's principle of superposition. The phase of each wavelet is distorted uniquely depending on the transmission path through the phase screen. Thus, the transmitted wave will be perturbed in phase differently at different points along the wavefront, but in this approximation, the phase differences will be small (less than a radian). The signal measured at Point P will be the superposition of the field of all wavelets integrated over the length of the transmitted wave. Amplitude fluctuations develop as a result of the diffraction of wavelets with phase irregularities. Thus, the generalized result is that the signal will be distorted in both phase and amplitude.

3. The Flat Plasma Spectrometer

Investigations into a novel technique to measure ionosphere/thermosphere parameters have culminated in the Flat Plasma Spectrometer (FLAPS) experiment, presently under development through a collaboration between NASA Goddard Space Flight Center (GSFC) and the United States Air Force Academy (USAFA). The motivation for the FLAPS experiment is driven by objectives that fall into both basic science and technology demonstration categories. Scientifically, there is strong interest in the effects of ionosphere-thermosphere coupling and non-thermalized plasma on the processes associated with equatorial F region ionospheric plasma bubbles. These bubbles have been known to scintillate transionospheric propagation of radio waves, often resulting in disruptions of communication and navigation systems. FLAPS investigations will assist in quantifying the impact of various processes on the instigation or suppression of plasma bubbles; certain outstanding questions include:

1. What is the relevance of meridional winds in suppression of plasma bubble growth?
2. What role does a velocity space instability driven by non-thermalized plasma play in the generation of small scale (<1 km) bubbles?
3. What process is responsible for turbulence in plasma beyond the edges of a bubble structure?

Technologically, the need for small yet capable instruments arises from the desire to make multipoint *in situ* measurements of "microscopic" plasma parameters to provide insight into "macroscopic" phenomena. Examples include coherency of spatial boundaries of large-scale (~ 100 km) plasma bubbles, three dimensional structure of the equatorial wind and temperature anomaly, and vertical velocity gradients in the low latitude ionosphere. The FLAPS design utilizes the state of the art in microfabrication of sensor head components for charged particle optics, Application Specific Integrated Circuits (ASICs) for charge amplification, a radiation hardened microcontroller for smart instrument

commanding, and a new ultra-low power high voltage power supply to drive the ionization filament.

FLAPS is capable of providing measurements of the full neutral wind vector, full ion-drift velocity vector, neutral and ion temperatures, and deviations from thermalization. In addition, course mass spectroscopy is possible using an energy analysis technique. The suite of instruments is comprised of a set of 16 individual neutral and ion analyzers, each of which is designed to perform a specific function. Advances in miniaturization technology have enabled a design in which the entire sensor package, including analyzers, ionization source, charge multiplication, and power supplies, requires a volume of 200 cm^3, power of 1.5 W, and a mass of 500 g. The suite requires a +5V regulated power line from the spacecraft, and the telemetry interface is a 3.3V TTL serial connection. Data collection rates vary from 1 to 1000 (192 Byte) "spectra" per second. The following description provides an overview of the instrument design of the FLAPS experiment.

The FLAPS Design

The basic FLAPS instrument concept is illustrated in Figure 12. Each tile represents an energy analyzer in the form of a bandpass filter with a unique look direction. From the figure, one can view the layout of the layers of the instrument sensor head. The collimator is used to select a look direction (represented by the colored cones) unique to each individual analyzer. The energy selector is then used as a band-pass filter to image plasma spectra differential in energy. The MicroChannel Plates (MCPs) provide charge multiplication to increase the sensitivity of the instrument. Finally, the Anode and Pre-Amplifiers/Discriminators (PADs) are then used to collect the resulting current and process the signal that will be stored by the instrument electronics assembly.

Figure 13 illustrates a SIMION run of ion trajectories as they traverse the FLAPS energy selector. P is the "Plate Factor", also known as the "Analyzer Constant", which is a measure of the amount of voltage required to be applied to the selection channel to resolve particles of a particular energy range. For example, with a P = 5, if we wanted to measure ions in a band with a central energy of 1 eV, we would have to apply 1.0 V/5 = 0.2 V across the plates; for 10 keV ions, we require 10 kV/5 = 2 kV, and so forth. Thus, to maintain relatively low plate voltages, we would want to make use of a variety of analyzer constants. For the FLAPS design, this is a function of the L/D (length over depth) ratio and the fractional width of the entrance slit, quantified by f = 1 - fraction of depth occupied by the slit (see Figure 13). Quantitatively, this is represented as an analytic function:

$$P = (1/4f)(L/d)^2$$

Another important factor for any electrostatic analyzer is the energy resolution, or ΔK/K, where ΔK is the width of the channel at half the maximum intensity and K is the passband central energy. This is a function exclusively of the fractional slit width, represented quantitatively as:

$$\left(\frac{\Delta K}{K}\right)_{FWHM} = \frac{4f(1-f)}{(3f^2 + 2f - 1)}$$

For example, with an f = 0.9, representing a slit that is 10% of the total depth of the channel, the FLAPS energy resolution is 11%.

Figure 14 illustrates the FLAPS ion drift/neutral wind meter concept. The yellow plates represent the entrance aperture and detector plane of a wind/temperature sensor moving to the right at supersonic velocity $\mathbf{V}_{SC}$ in the upper atmosphere, where the mean free path is long compared to the dimensions of the spacecraft. The air stream passing the entrance aperture spreads out in angle due to the thermal random velocity of the air, giving the angular distribution pattern shown in red on the detector plane. Careful measurement of this angular distribution gives the temperature of the air and the component of the wind perpendicular to $\mathbf{V}_{SC}$. If the energy spectrum at the peak of the distribution were known, the total wind velocity vector could be obtained.

Figure 15 shows the method of velocity vector determination. Red lines represent angular scans of plasma spectra using two mutually perpendicular drift meters. Once the two simultaneous angular measurements are made

along perpendicular planes, the angles of maximum flux in each of these planes gives the distance of the corresponding measured energy distributions from the peak in the angular distribution. These two angles may then be used with the energy spectra to obtain the total velocity vector. Once the peak in the ion distribution (in angle) is determined in the 2D plane, the 3D velocity vector can be obtained by resolving the peak in the energy distribution. This is accomplished by a sweep in energy.

Figure 16 illustrates the energy distribution at the peak of the angular distribution for a realistic atmosphere. The figure on the left shows a semi-logarithmic plot of the atom-molecule flux as a function of energy at the peak of the angular distribution. The linear plot of the figure on the right shows two distinct flux maxima corresponding to the principal constituents O and N_2. The energy of these constituents differs by virtue of their mass since both enter the detector with velocity very close to V_{SC}. In this sense, the energy analysis of the air stream may be used for coarse mass analysis of the major species. More detailed studies were done with noise added to simulate the measured spectra with some realism. These demonstrate that it is possible to infer the energies of He, O, N_2/O_2 , and Ar, independently, once the peak of the angular distribution is known. A non-linear least-squares-fit technique was implemented to analyze these data.

The neutral wind and ion drift meters are founded upon a single charged-particle spectrometer geometry selected for its compactness and ability to provide the required sensitivity and energy-angle resolution (see Figure 17). An array of parallel plate energy analyzers is used to obtain the angular and energy distributions of the air atoms and molecules; each energy analyzer is tilted at an angle to define the angle of incidence of the air stream. In this design each sensor uses 11 look angles: -10° to +10° in 2° intervals. The FLAPS experiment to be flown on USAFA's FalconSAT-3 spacecraft will only sample over 5 angular channels. Each analyzer has its own entrance slit, but this is not sufficient to restrict the trajectories sufficiently to make it possible to have a unique energy corresponding to the analyzer voltage. The entrance aperture at the top serves to define the range of angles of incidence of each analyzer.

Figure 18 illustrates a sample configuration of a FLAPS suite that houses 16 unique analyzers. Included in this complement are:

- 9 Spectrometers, with P = 6, 10° off-vertical, variable azimuth
- 4 Ion drift/neutral wind meters
- 3 "engineering" experimental analyzers (*e.g.*, special coatings, various analyzer constants and look directions)

The nominal dimensions are:

- Cylindrical Sensor Head (7cm diameter x 1.3 cm height)
- Electronics box $(7\text{ cm})^2$ x 2.7 cm

Thus, the total instrument envelope, including electronics, is of a 7 cm × 7 cm × 4 cm rectangular volume.

The aluminum electronics box contains the FLAPS microcontroller, an HV power supply, ASICs, and an FPGA serial translator. The mounting bracket is fastened to electronics box for bolting the instrument to the spacecraft surface. A 19-pin NANONICS connector will provide the main electrical interface, including power, digital control, and serial telemetry lines.

4. Challenges in Miniaturization

One of the most challenging aspects in spacecraft miniaturization is the limited (albeit growing) availability of miniaturized Commercial Off The Shelf (COTS) subsystem components. Consider the subsystems required to support a 10 kg spacecraft capable of meaningful research. Minimum requirements include power, command and data handling, transceiver, microcontroller, a payload, and a structure robust enough to withstand a launch environment. Many experiments require additional subsystems, including attitude determination and control, orbital maneuvering, *etc.* Furthermore, construction of miniaturized structures requires processes that are not necessarily feasible or practical using true Micro Electromechanical Systems (MEMS) technologies. Finally,

component miniaturization faces significant challenges associated with radiation hardness. With this section, we examine the present state of availability of enabling subsystems and processes and areas of need for the future.

Surrey Satellite Technology Ltd (SSTL) has demonstrated their Surrey Nanosatellite Applications Platform (SNAP) with the 6.5 kg SNAP-1 spacecraft. SNAP-1 was developed with a VHF uplink, S-Band downlink (76.8 kbps), a StrongARM onboard computer (4 MB EDAC memory), a CAN bus for data handling, three-axis attitude determination and control, a GPS receiver, power subsystem (4W/9W average/peak), and a CMOS camera that served as its primary payload. The satellite was successfully deployed on 28 June 2000, and demonstrated immediate functionality by completing a 60 second imaging sequence of its own deployment, commencing two seconds upon separation from the deployer platform [*SSTL*, 2000]. Demonstration of this system shows promising results for miniaturized spacecraft.

One of the most significant enabling processes supporting miniaturization of spacecraft components, especially those of a structural nature, has been the advancement of various forms of Micro/Meso Mechanical Manufacturing, or M^4, technology. *Fox et al.* [2000] presents a useful overview in which many of the latest processes are described. Focused ion beams, used to ablate materials through kinetic energy transferred to the material, can be used to attain feature size down to ~200 nm in structures of arbitrary material. Micro-milling and -turning is used to achieve 25 μm features in common materials, such as plastics, aluminum, stainless steel, *etc*. Excimer lasers are used to achieve feature sizes down to 6 μm, but are more efficient for structures of polymers and ceramics than for metallic structures. Micro-Electron Discharge Machining (Micro-EDM), which uses a fine (radius ~ 1 mil) electrode to generate sparks that ablate material from conductive surfaces, is used to attain features of 25 μm. These processes and others are key to the manufacturing of structures necessary to support miniaturized satellites that support meaningful research projects. In particular, construction of the FLAPS necessitates the use of Micro-EDM.

It is well known that the tendency for reduction in feature size (*e.g.*, gate length) within electronics devices results in an increased sensitivity to SEUs. For gates of shorter length, the Linear Energy Transfer (LET), corresponding to the amount of charge created per unit path length required for an SEU, is significantly less. Quantitatively, for a feature size (~ 1 μm) reduction by a factor of 2, the threshold LET for an SEU is reduced by a factor of 5 (see Figure 19). Additional complications arise through the development of smaller and faster memory, such as an SRAM cell. Since the area of the cell forming the capacitive plates is reduced, the memory cell capacitance itself is reduced. If one were to apply a resistive decoupling technique to harden the SRAM against SEE, the feedback resistance must be increased (*e.g.*, in excess of 100 kΩ for high density SRAM) to compensate for the reduction in capacitance.

6. Concluding Remarks

With this paper, we have presented a brief overview of space environmental conditions and processes of interest to those who rely on systems that are potentially affected by space weather. Though substantial progress has been made in the area of enabling technology, numerous challenges remain. Among the significant challenges that were not addressed in this paper, perhaps the most serious is the limited availability of launch opportunities for such miniature spacecraft. Ideally, we anticipate that groups of miniature satellites may be launched with a single flight. However, reasonable separation into a 3D spatial grid necessary for an operational space weather constellation mandates a potent orbital maneuvering system, something capable of inducing altitude, phase, and plane changes. Breakthrough propulsion techniques may be necessary for a viable operational space weather constellation.

7. References

Barker, T. G., Analytic and Observational Approaches to Spacecraft Auroral Charging, *AFGL-TR-87-0021*, ADA181456, 1986.

Binder, D., E. C. Smith, A. B. Holman, Satellite anomalies from galactic cosmic rays, *IEEE Trans. Nuc. Sci., v. NS-22*, n. 6, p. 2675, 1975.

DeForest, S. E., Spacecraft Charging at Synchronous Orbit, *J. Geophys. Res., v. 77*, p. 651, 1972.

Fontheim, E. G., K. Stasiewicz, M. O. Chandler, R. S. Ong, E. Gombosi, and R. A. Hoffman, Statistical Study of Precipitating Electrons, *J. Geophys. Res., v. 87*, n. A5, p. 3469, 1982.

Frederickson, A. R., S. Woolf, J. C. Garth, Model for Space Charge Evolution and Dose in Irradiated Insulators at High Electric Fields, *IEEE Trans. Nuc. Sci., v. 40*, p. 1393, 1993.

Habash Krause, L., B. K. Dichter, D. J. Knipp, K. P. Ray, The Relationship between DSCS III Sunlit Surface Charging and Geomagnetic Activity Indices, *IEEE Trans. Nuc. Sci., v. 47*, n. 6, p. 2224, 2000.

Knipp D. J., T. Welliver, M. G. McHarg, F. K. Chun, W. K. Tobiska and D. Evans, Climatology of Extreme Upper Atmospheric Heating Events, *Adv. Space Res.*, **submitted**, 2002.

Kolasinski, W. A., J. B. Blake, J. K. Anthony, W. E. Price, E. C. Smith, Simulation of cosmic-ray induced soft errors and latchup in integrated-circuit computer memories, *IEEE Trans. Nuc. Sci., v. NS-26*, n. 6, p. 5087, 1979.

Mizera, P. F., Natural and Artific ial Charging: Results from the Satellite Surface Potential Monitor Flown on P78-2, *AIAA 80-0334*, AIAA 18th Aerospace Sciences Meeting, AIAA Press, New York, 1980.

Mullen, E. G., M. S. Gussenhoven, D. A. Hardy, T. A. Aggson, B. G. Ledley, and E. Whipple, "SCATHA survey of high-level spacecraft charging, *J. Geophys. Res., v. 91*, n. A2, p. 1474, 1986.

NSWP, The National Space Weather Program: The Implementation Plan, 2nd Edition, http://www.ofcm.gov/, July 2000.

SSTL, http://www.surrey.ac.uk/news/releases/10-0100sstl.html, 2000.

Waskiewicz, A. E., J. W. Groninger, V. H. Strahan, D. M. Long, Burnout of power MOS transistors with heavy ions of Californium-252, *IEEE Trans. Nuc. Sci., v. 33*, n. 6, p. 1710, 1986.

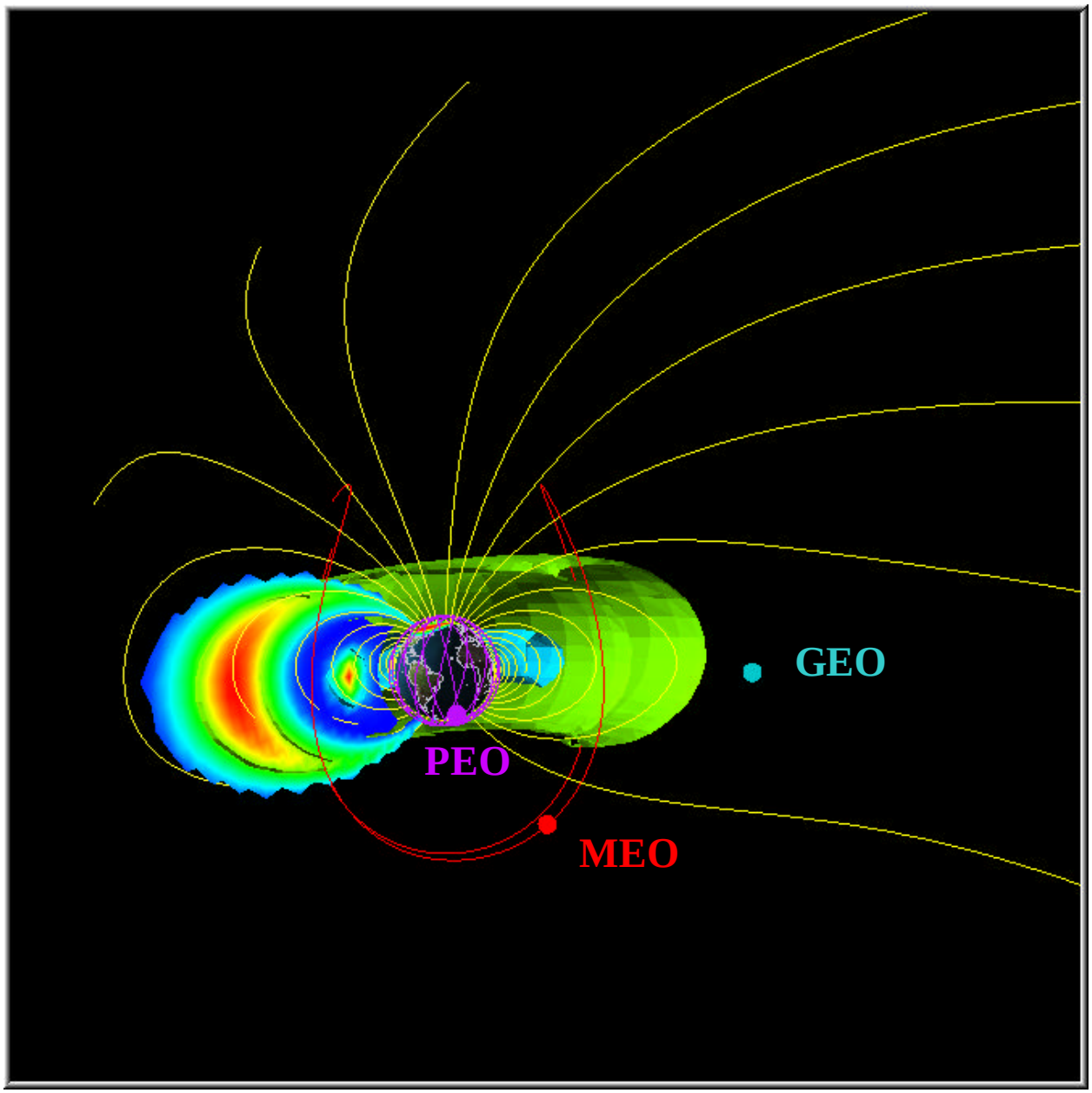

Figure 1. An overview of the near-Earth space environment. Terrestrial magnetic field lines are shown in yellow; inner and outer Van Allen radiation belts are shown with color intensity plots (with red=maximum), each with a sample isosurface. Three typical satellite orbits are shown for reference: Geosynchronous Earth Orbit (GEO), Medium Earth Orbit (MEO), and Polar Earth Orbit (PEO). Note that the GEO is typically beyond the outer edge of the outer belt, the MEO traverses the heart of the outer belt, and the PEO intersects the cusp region of the inner belt.

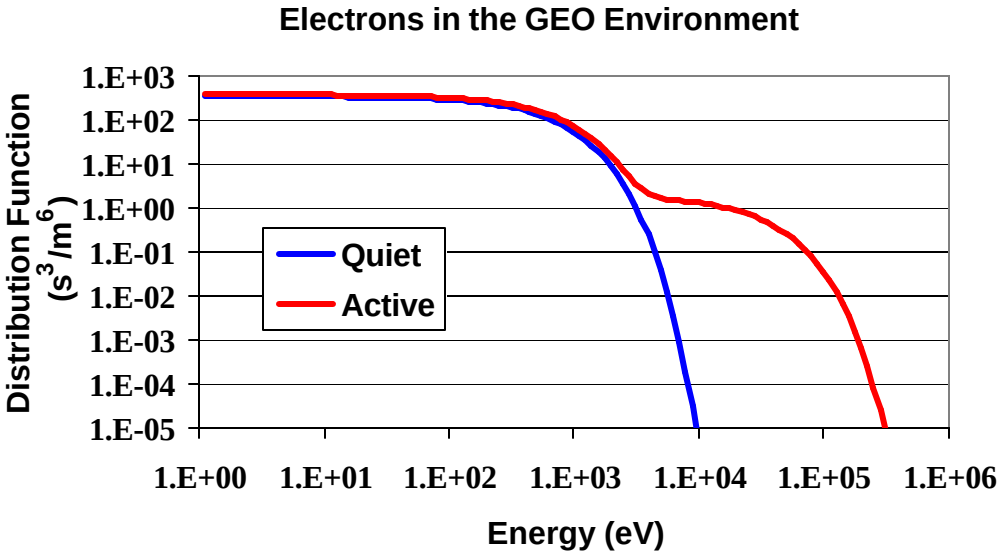

Figure 2. Specification of a GEO plasma during quiet and active periods. During significant geomagnetic activity, it is more appropriate to specify the electron population as a two temperature Maxwellian. Parameters of the two-temperature Maxwellian are 1) Quiet: kT_1 = 550 eV, kT_2 = 9.0 keV; Active: kT_1 = 600 eV, kT_2 = 25 keV.

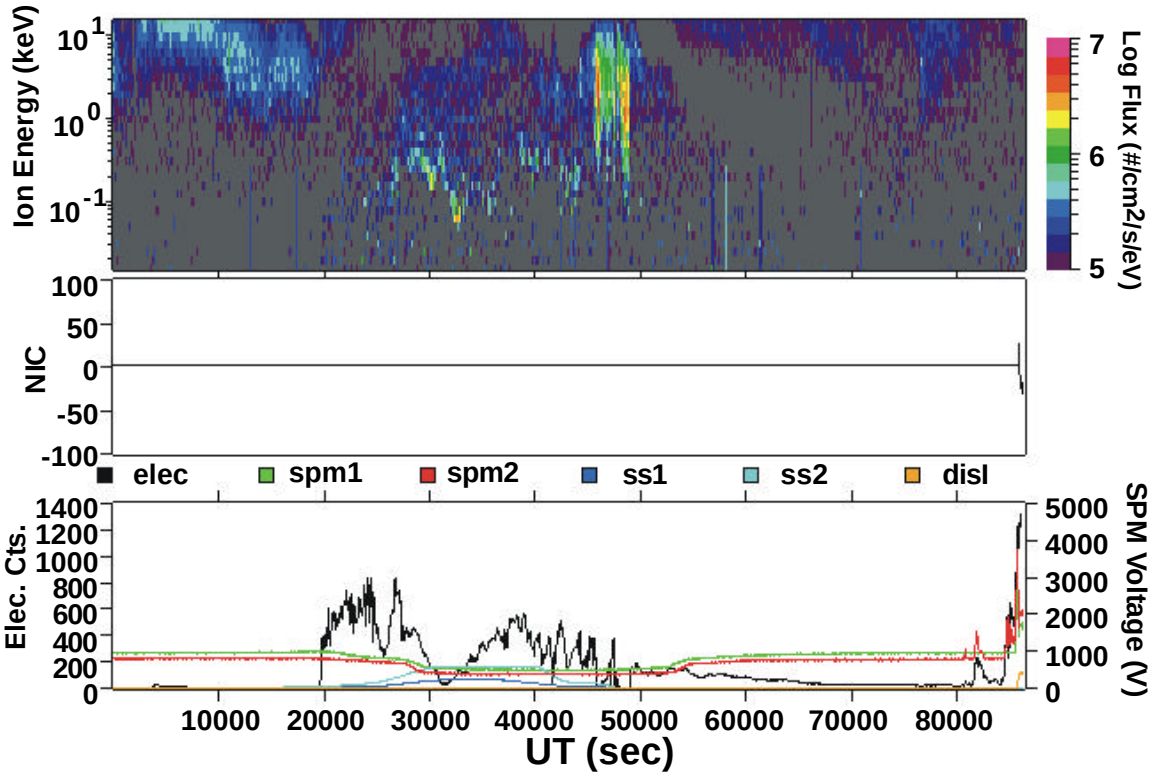

Figure 3. A GEO satellite within the Defense Satellite Communication System (DSCS III) constellation experience direct exposure to solar wind particles between UT = 46000 and 49000 seconds, as evident by the ion flux measurements illustrated in the top panel. Energetic electron injection is evident by the bulk count rate summed over the 20 keV to 50 keV channels shown in the bottom panel with the black curve.

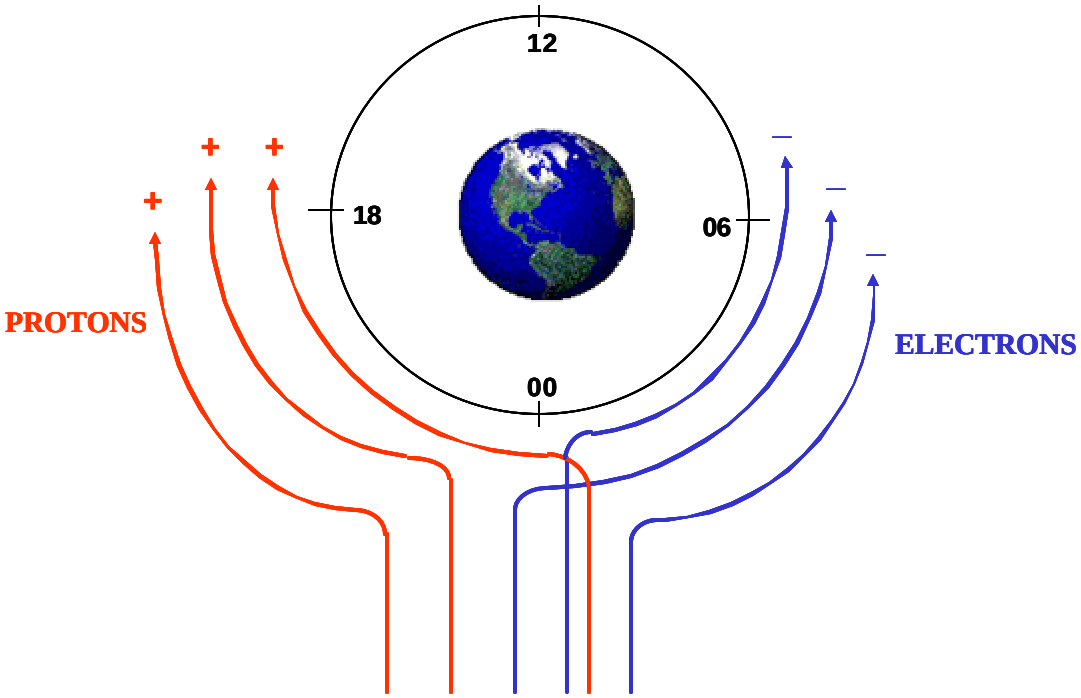

Figure 4. Energetic charged particle entry from magnetotail into the geosynchronous environment. Note that the electrons are injected into the post midnight sector, whereas the ions are injected into the pre-midnight sector. A net westward current results.

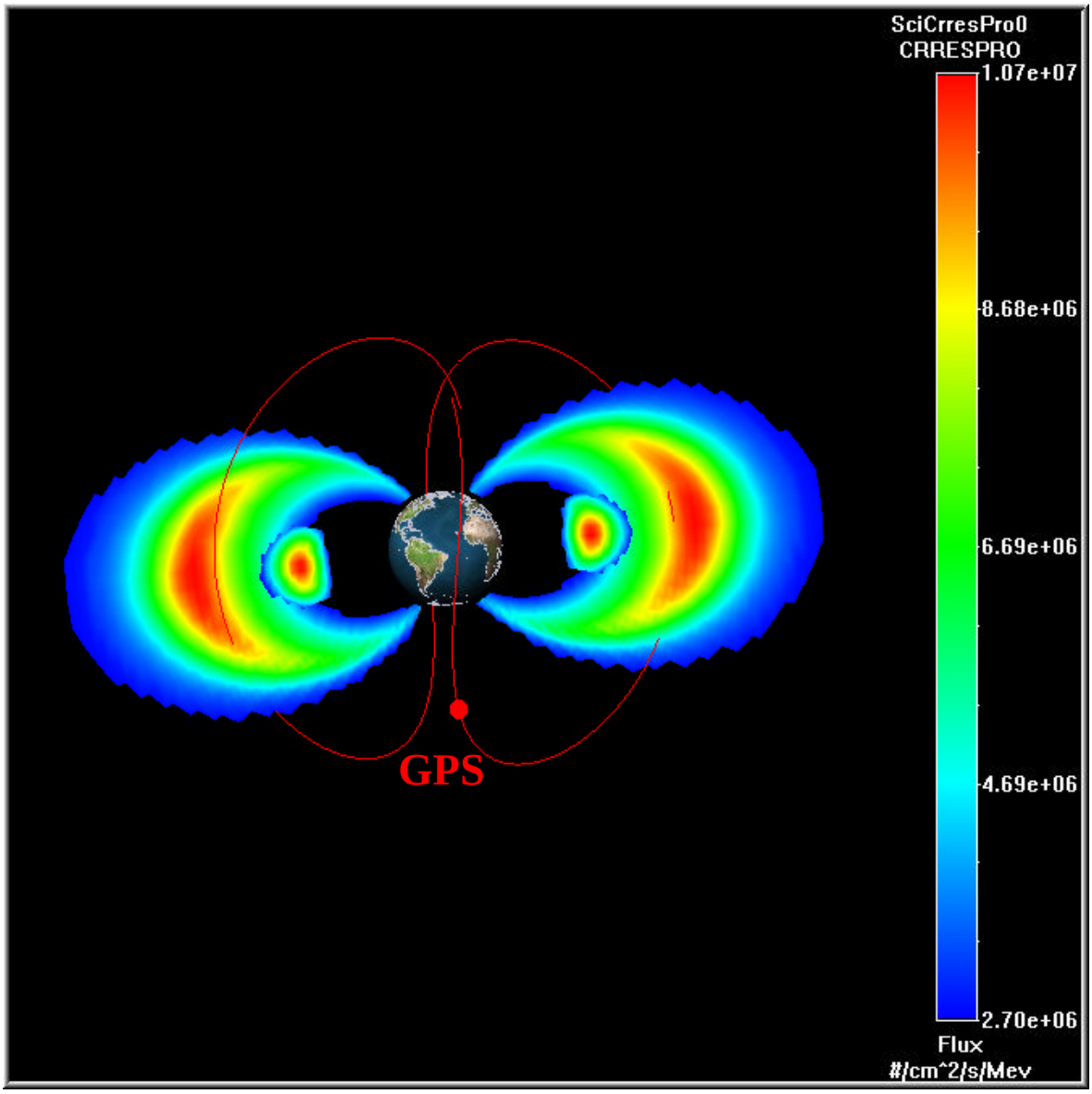

Figure 5. Sample MEO orbit transiting the heart of the outer radiation belt.

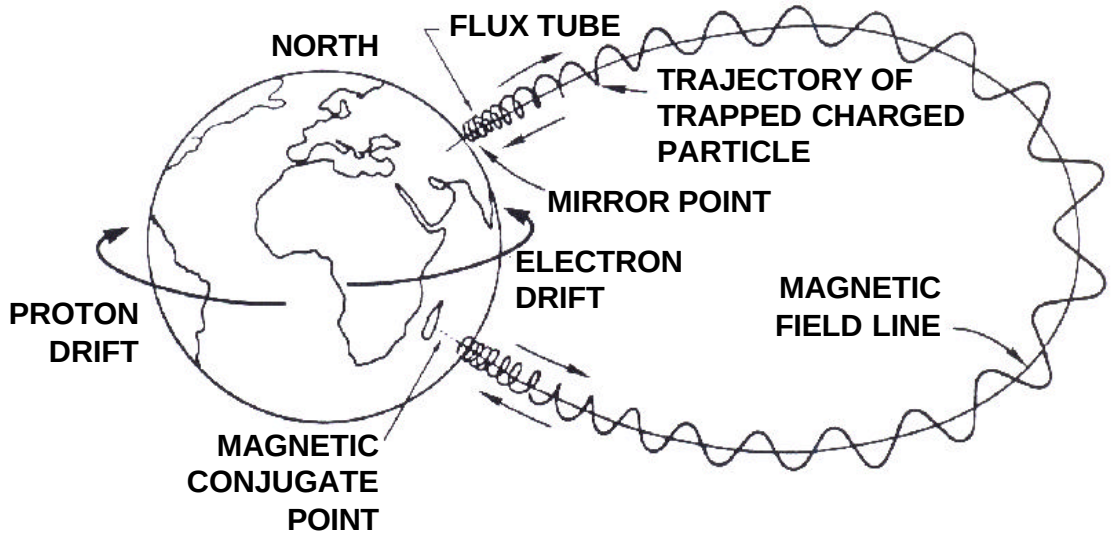

Figure 6. Overview of single particle trajectories in the magnetosphere.

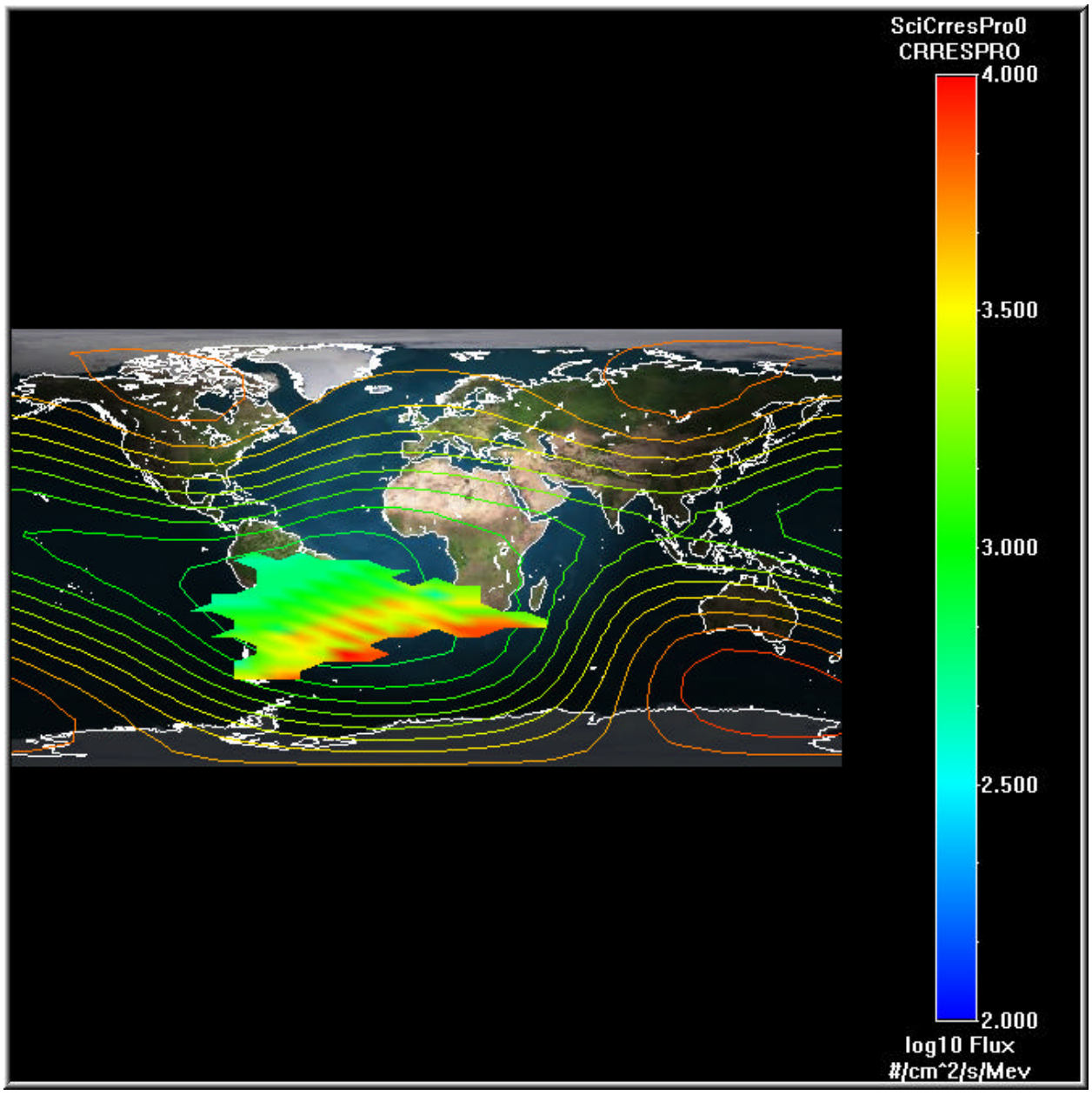

Figure 7. The South Atlantic Anomaly (SAA) is shown with colored isocontours (with red = maximum) of the Earth's magnetic field computed using the International Geophysical Reference Field (IGRF) 1995. The color intensity plot represents 1 MeV proton flux at 630 km in altitude.

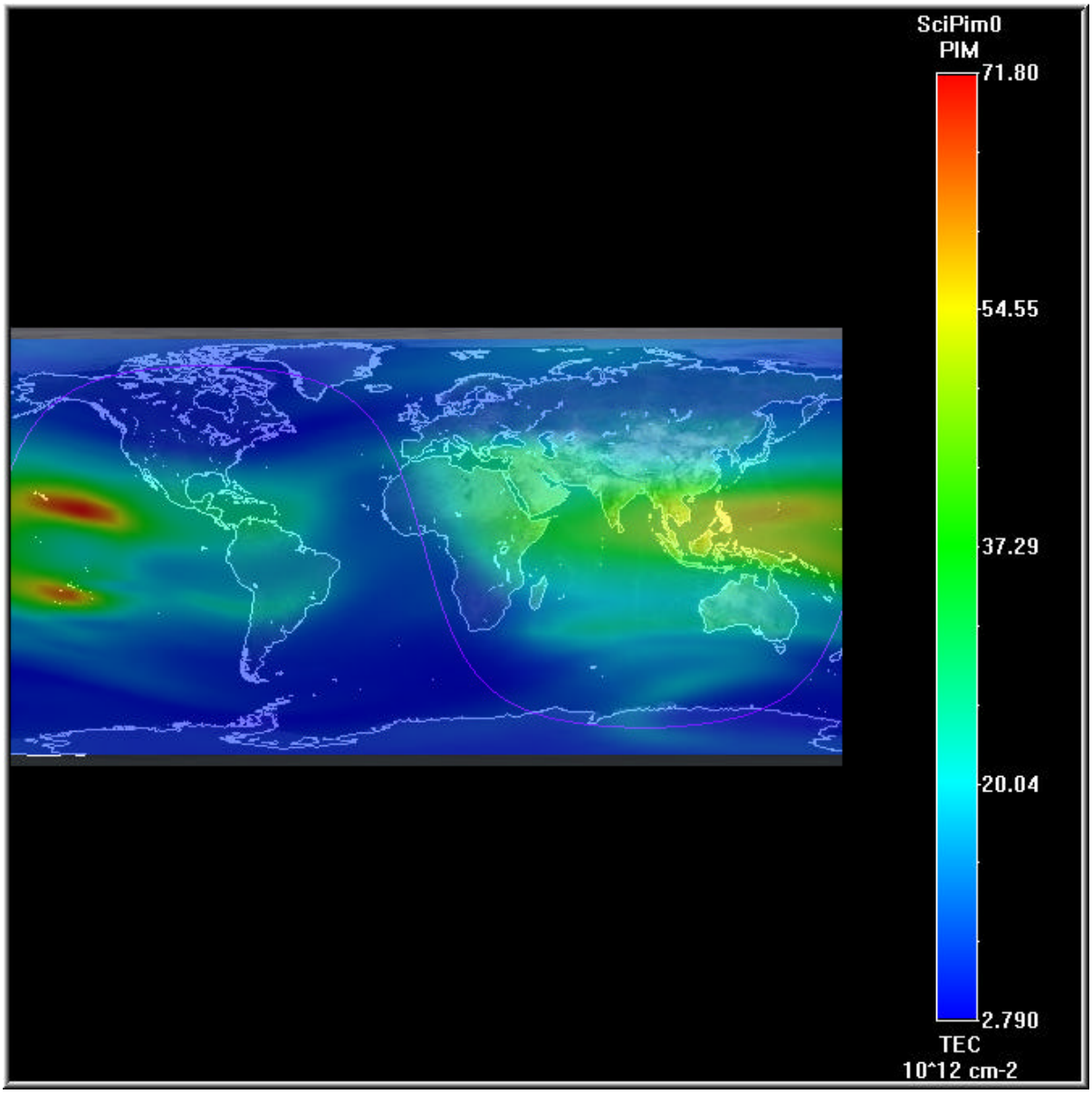

Figure 8. The Equatorial Appleton Anomaly describes peaks in plasma density concentrated in two bands in latitude, as illustrated with this color intensity plot of Total Electron Content (TEC).

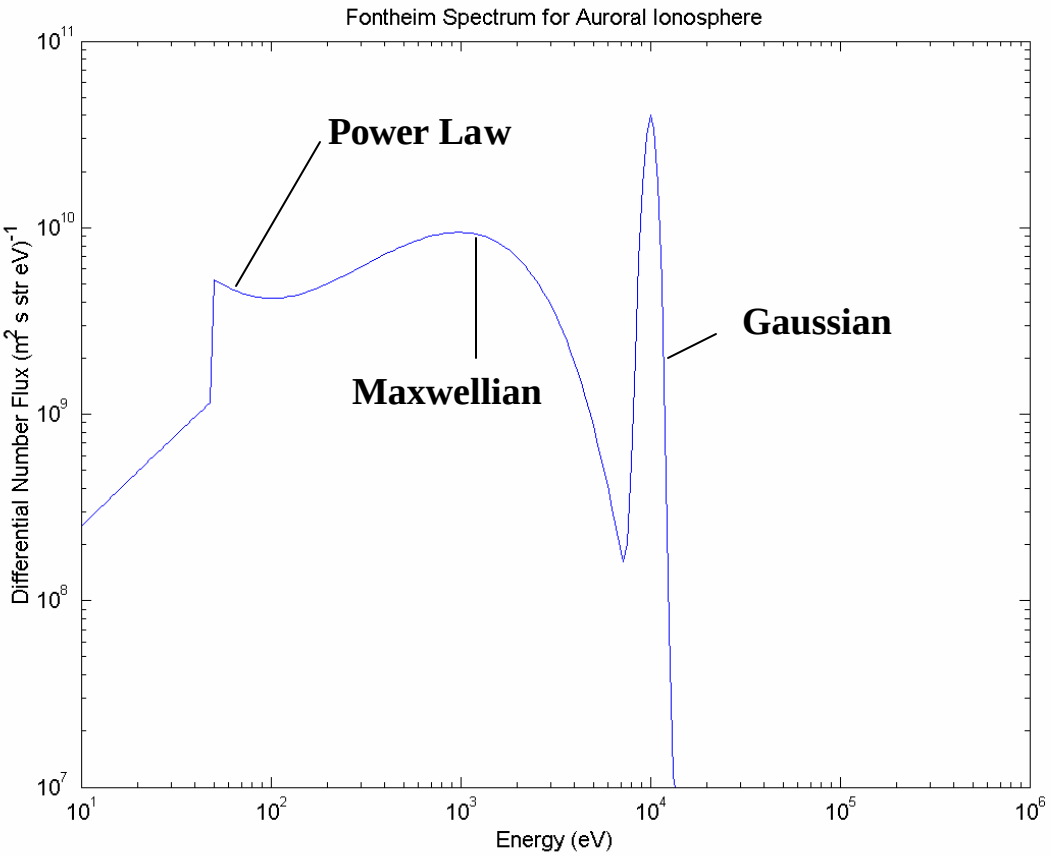

Figure 9. Fontheim spectrum for A_P=3 ´ 10^{11} m^{-3}, A_G=4 ´ 10^4 m^{-3}, a = 1.1, E_{PL} = 50 eV, E_{PH} = 1.6 ´ 10^6 m^{-3}, n_e=6 ´ 10^5 m^{-3}, kT = 1.0 keV, Eo = 10 keV, D = 1.0 keV.

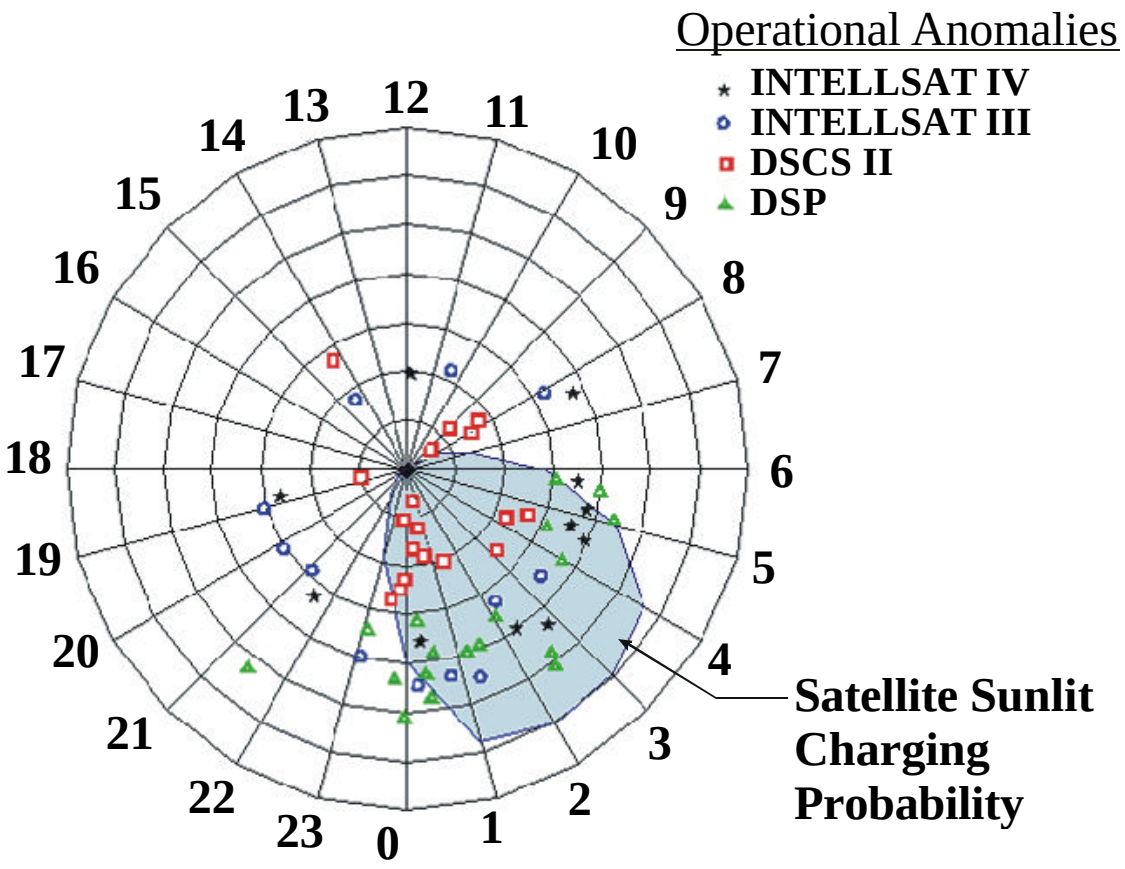

Figure 10. GEO Satellite operational anomalies are shown with markers to categorize by constellation. The sunlit charging probability is overlaid as a polar plot, with each subdivision representing 5% probability that a satellite will charge to at least 50 V negative with respect to the background plasma during its transit of the post-midnight sector.

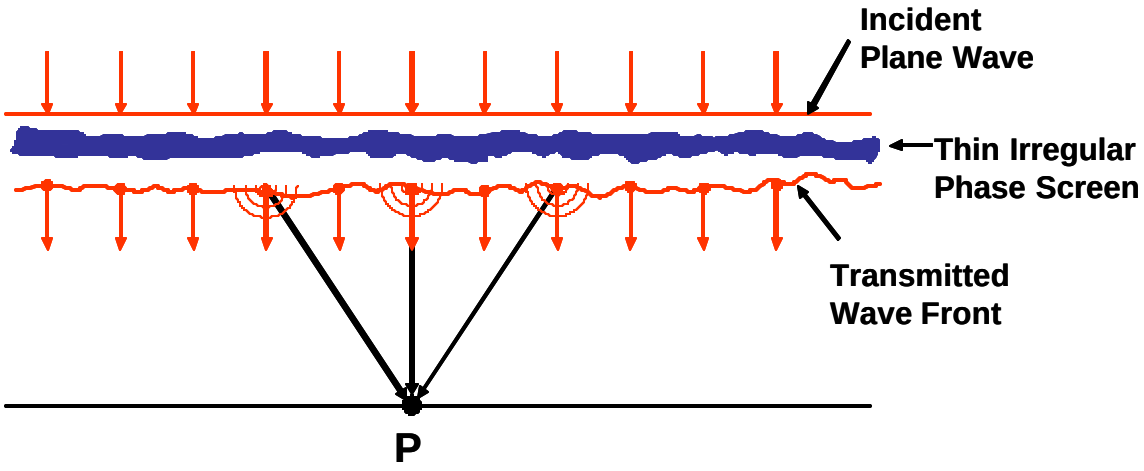

Figure 11. Scintillation of plane wave resulting from transmission through infinitely thin irregular surface. This represents the so called Phase Screen Approximation of scintillation theory.

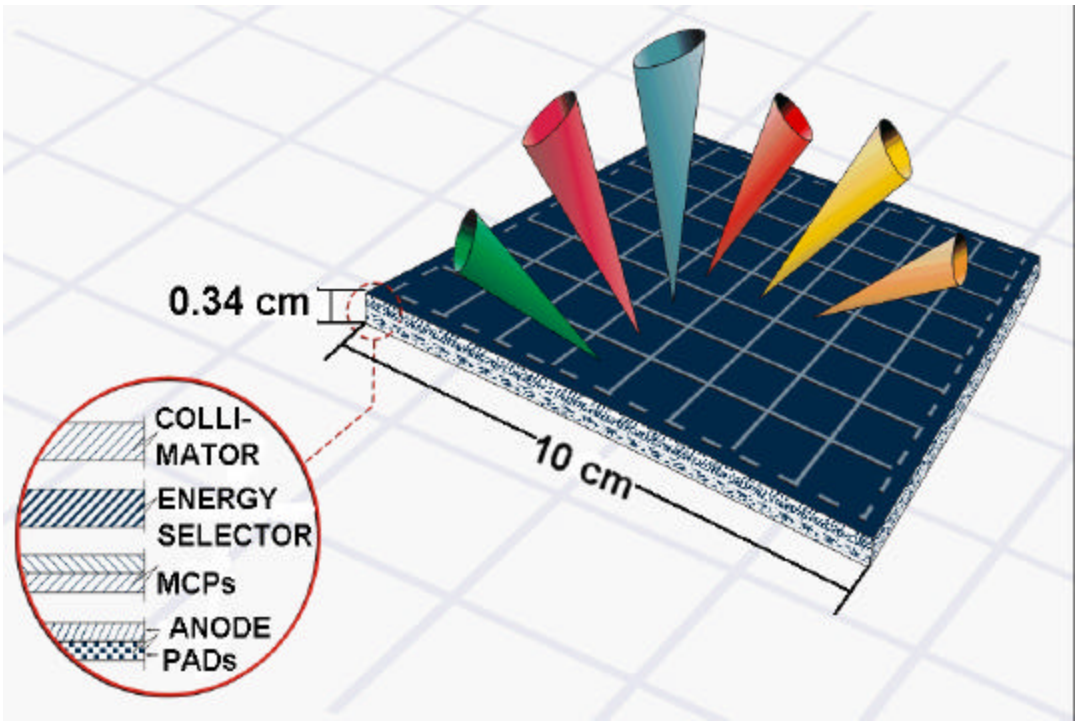

Figure 12. FLAPS Conceptual Illustration: 8 by 8 array, where each tile has unique look-direction, analyzer constant, coating, etc.

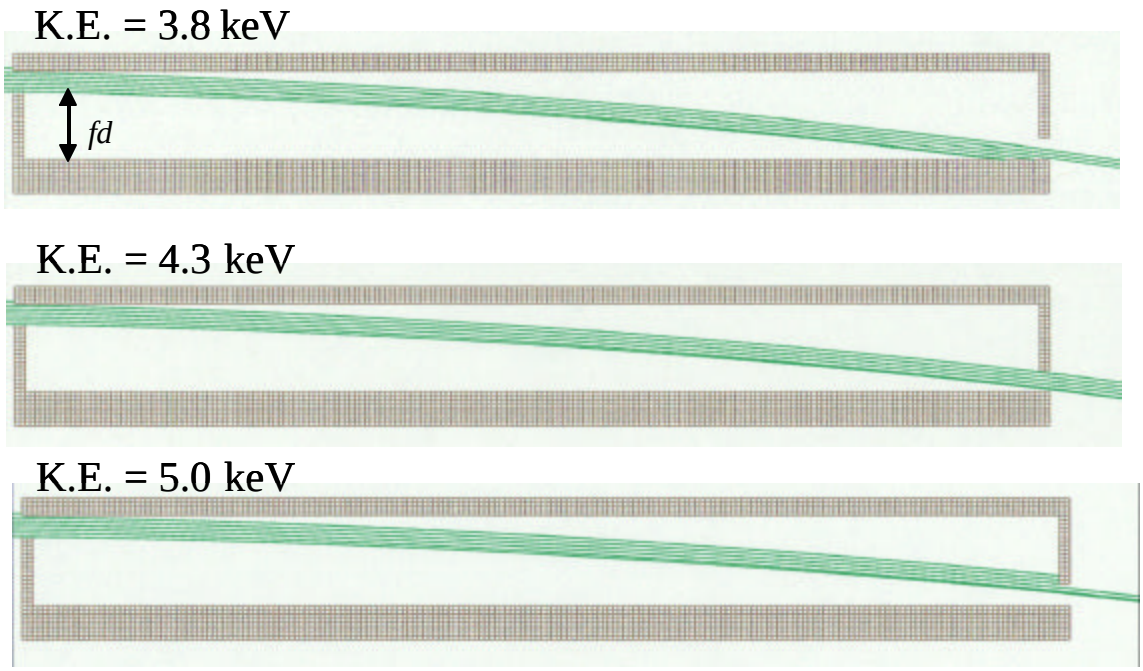

Figure 13. SIMION simulated trajectories of ion energy analysis in the FLAPS energy bandpass filter. Ions enter through the slit in the top left corner of the channel and are bent by a downward electric field. The top panel represents trajectories for energies on the lower end of the energy passband; the middle panel represents trajectories for ion beam energies with channel central energy, and the bottom panel represents trajectories for energies at the higher end of the energy passband.

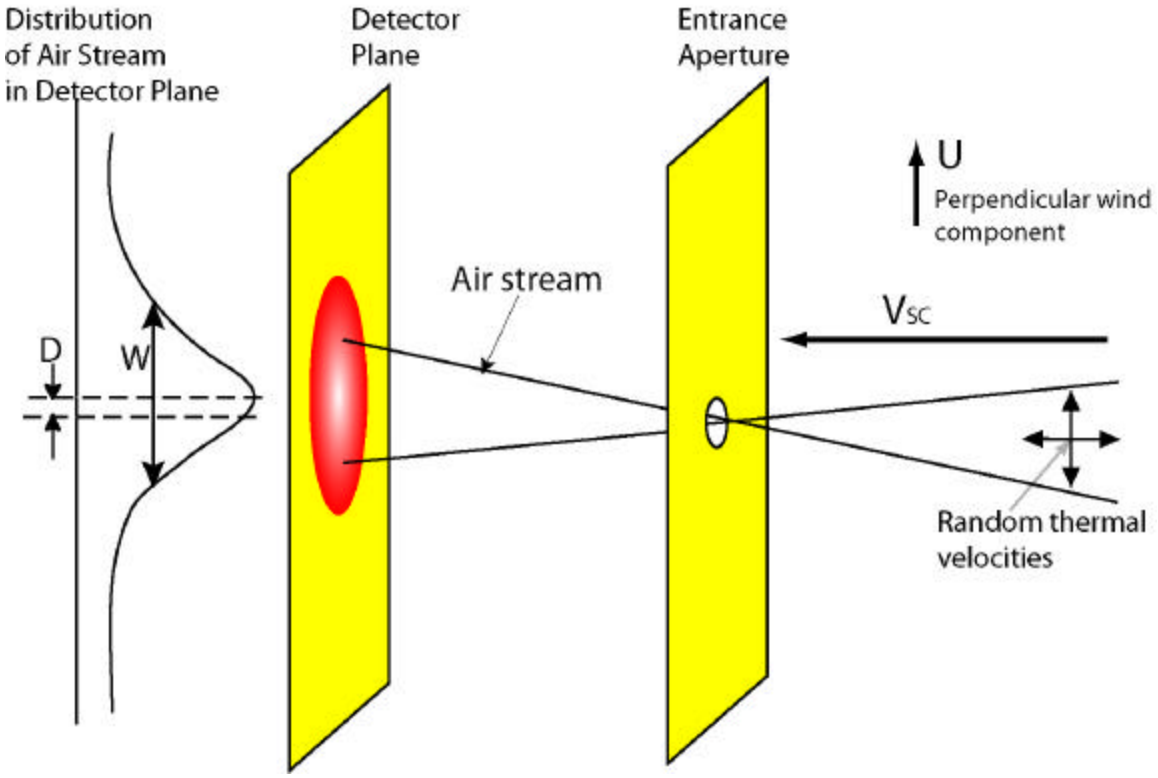

Figure 14. The FLAPS drift meter concept. See text for details.

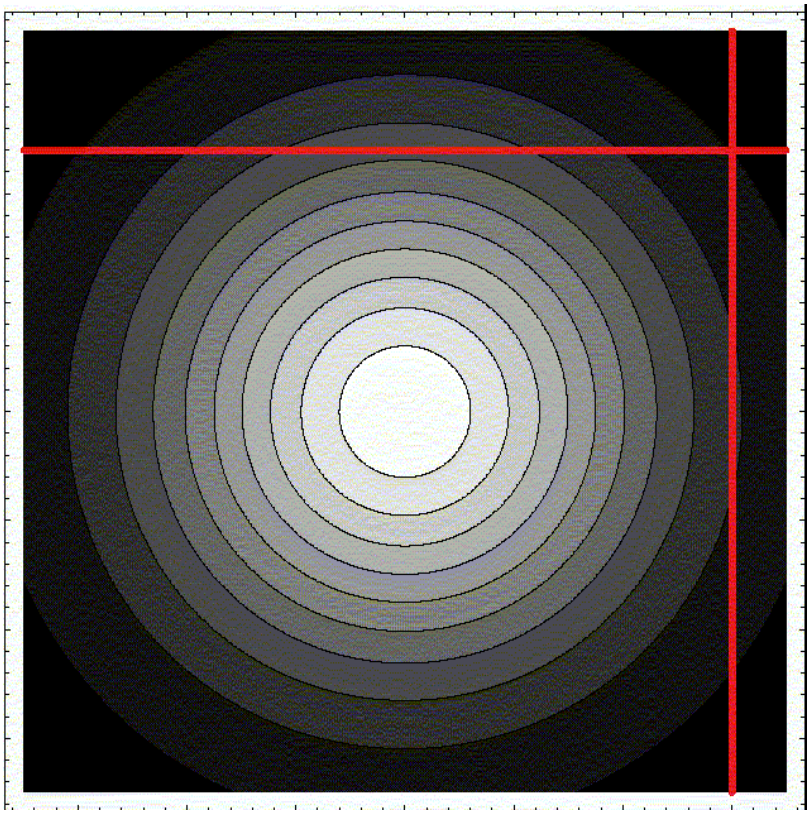

Figure 15. Determination of the peak of the angular distribution simultaneous with the energy distribution. See text for details.

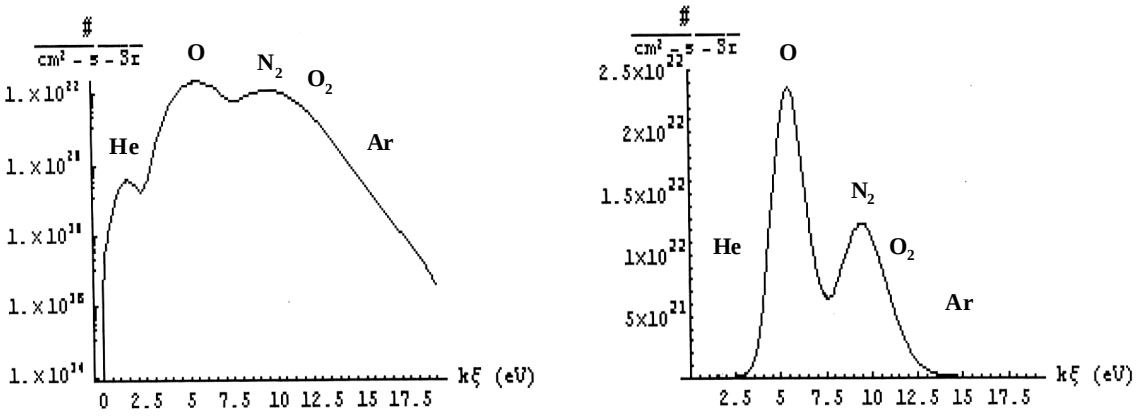

Log Plot ⇒ Major and Minor Constituents Linear Plot ⇒ O, N2

Figure 16. The energy distribution at the peak of the angular distribution is simulated here for a realistic upper atmosphere.

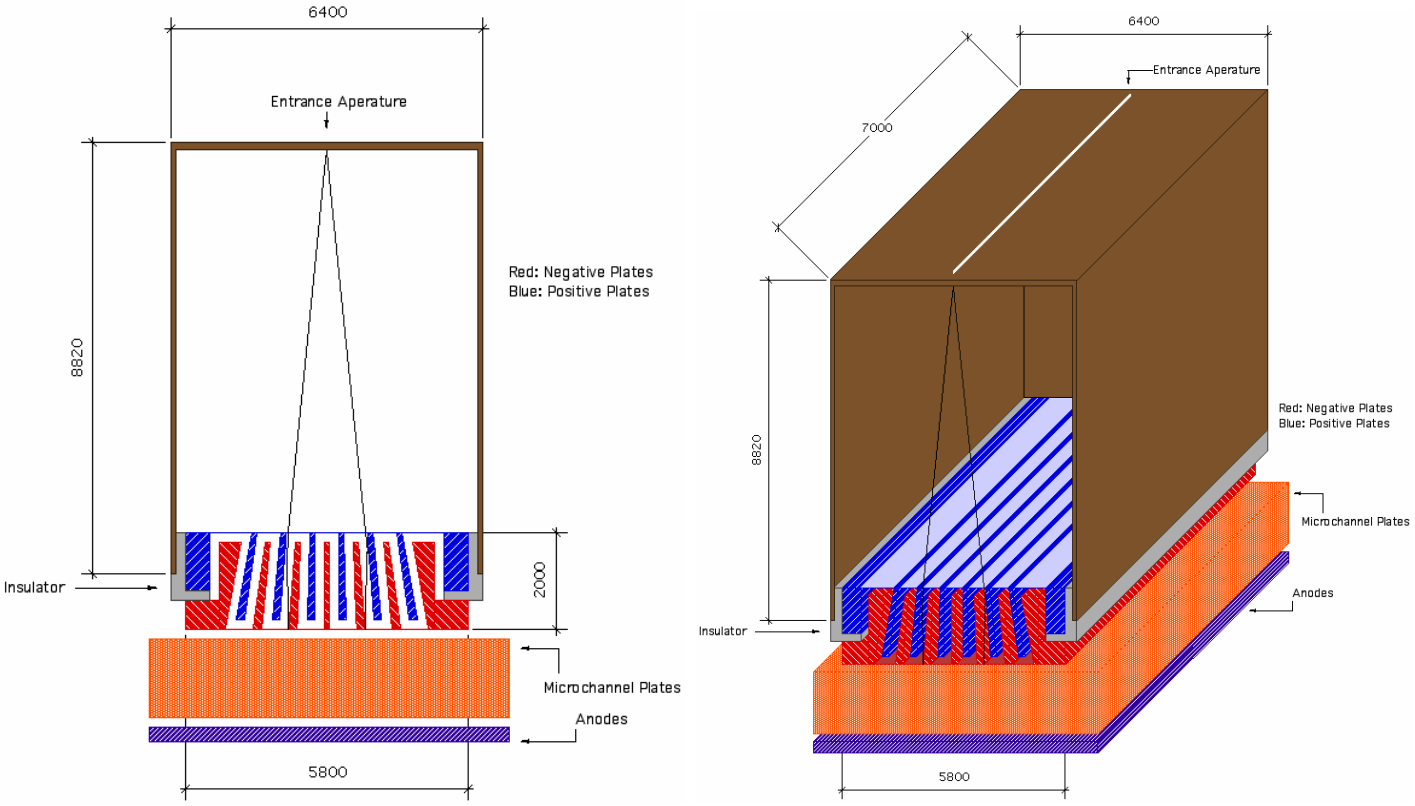

Figure 17. Ion drift and neutral wind meter design. Dimensions are in microns. See text for details.

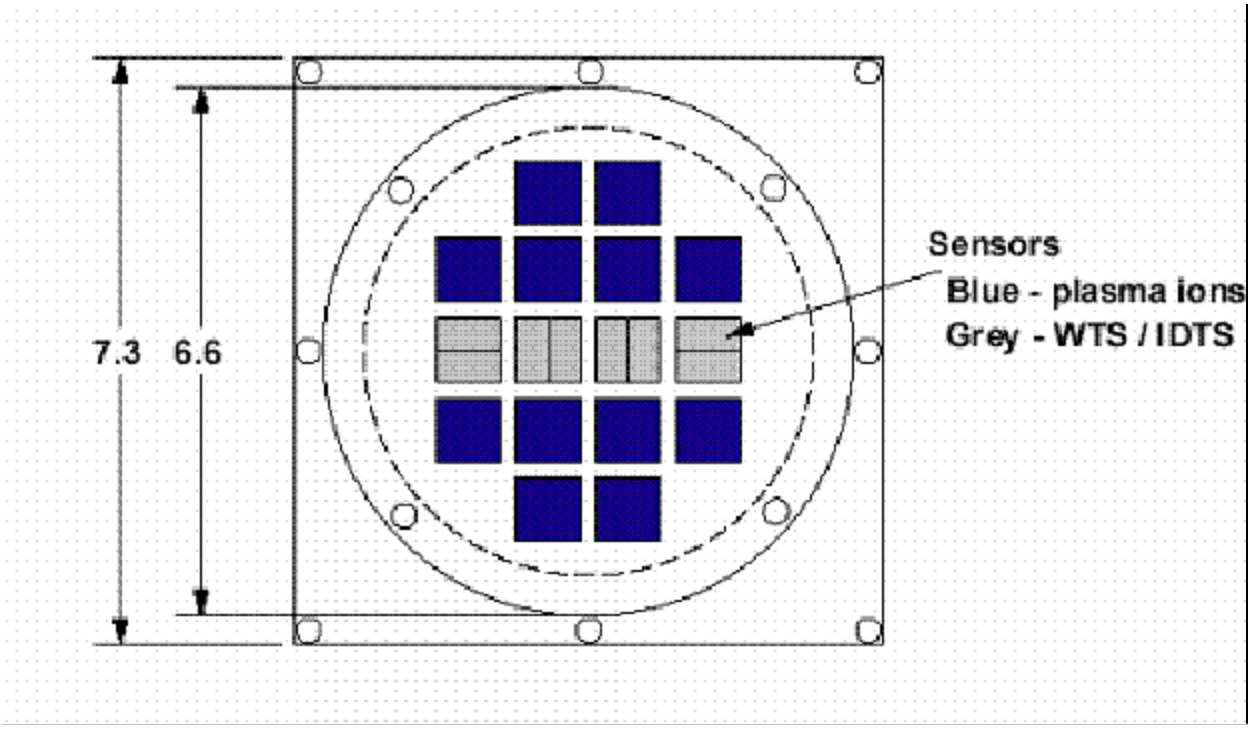

Figure 18. Top view of FLAPS suite with an arrangement of 16 analyzers. Dimensions are in cm.

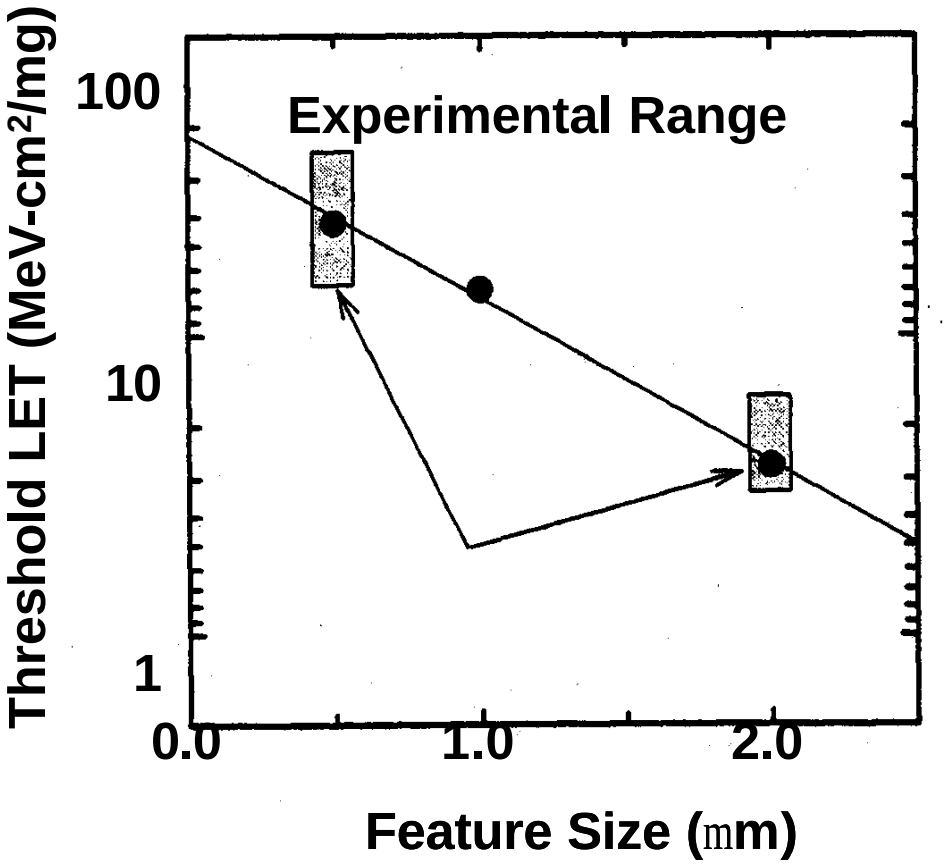

Figure 19. SEU threshold LET values are plotted versus SRAM feature size. Devices represented here are not radiation hardened.